Geophysical Research Letters

RESEARCH LETTER
10.1029/2022GL101441

Key Points:

- Fluid transported and mixed by vertically migrating aggregations of plankton in the ocean has a distinct magnetic field signature
- The magnetic signature of biomixing is potentially detectable far from aggregations with emerging, quantum-enhanced magnetometry techniques
- The present approach avoids triggering animal avoidance behavior and does not require *a priori* knowledge of the precise aggregation location

Supporting Information:

Supporting Information may be found in the online version of this article.

Correspondence to:

J. O. Dabiri,
jodabiri@caltech.edu

Citation:

Fu, M. K., & Dabiri, J. O. (2023). Magnetic signature of vertically migrating aggregations in the ocean. *Geophysical Research Letters*, *50*, e2022GL101441. https://doi.org/10.1029/2022GL101441

Received 6 OCT 2022
Accepted 23 JAN 2023

Magnetic Signature of Vertically Migrating Aggregations in the Ocean

M. K. Fu[1,2] and J. O. Dabiri[1,2]

[1]Graduate Aerospace Laboratories, California Institute of Technology, Pasadena, CA, USA, [2]Department of Mechanical and Civil Engineering, California Institute of Technology, Pasadena, CA, USA

Abstract The significance of fluid transport in the ocean due to migrating aggregations of zooplankton remains poorly understood due to practical challenges associated with predicting, identifying, and quantifying instances of enhanced biogenic mixing. We present a new approach to overcome these limitations by quantifying the biogenic transport via its distinct magnetic signatures. This present approach can be accomplished potentially without *a priori* knowledge of the precise location of the aggregation and without triggering animal avoidance caused by the introduction of instruments into the migration.

Plain Language Summary Fluid transport by vertically migrating aggregations of plankton has long been explored as a potentially important source of ocean mixing. However, direct evidence of enhanced stirring remains inconclusive as current approaches require *a priori* knowledge of the precise aggregation location and typically trigger animal avoidance behavior from introducing instrumentation into the migration. This Letter proposes a new approach to overcome these longstanding limitations by measuring the magnetic signatures of biogenic transport. By leveraging modern magnetometry, especially quantum-enhanced techniques, magnetic measurements of biogenic stirring can be related to the integrated fluid flow and are potentially detectable remotely at distances far removed from the aggregation.

1. Introduction

Biologically generated mixing from vertically migrating aggregations of plankton remains a poorly understood mechanism by which heat and solutes are potentially mixed in the ocean (Dabiri, 2009; Dewar et al., 2006; Houghton et al., 2018; Wilhelmus & Dabiri, 2014). While the induced flow and stirring associated with an isolated animal occur at the scale of the swimmer (Visser, 2007), plankton often exist in dense swarms over 10s of meters in height and 100s of meters in width (Huntley & Zhou, 2004; Sato et al., 2013), and collectively traverse 100s of meters during their diel vertical migrations (Sato et al., 2013; Wiebe et al., 1979). The emergence of aggregation-scale mixing eddies comparable to the stratification length scales of the water column has been proposed as a potential mechanism through which vertically migrating aggregations can induce appreciable transport in the water column through which the organisms migrate (Dabiri, 2009; Kunze et al., 2006). Though recent studies provide evidence for such a mechanism (Houghton & Dabiri, 2019; Houghton et al., 2018; S. Wang & Ardekani, 2015; Wilhelmus & Dabiri, 2014), direct environmental measurements of enhanced stirring due to vertically migrating aggregations in lakes and the ocean have proven less conclusive and challenging to obtain (Kunze, 2019; Lorke & Probst, 2010; Noss & Lorke, 2014; Rousseau et al., 2010; Simoncelli et al., 2018). These challenges are due in large part to the practical difficulties associated with predicting, identifying, and quantifying instances of enhanced biogenic stirring in the environment (Fernández Castro et al., 2022), especially given the spatiotemporal patchiness of their occurrence in the ocean. Moreover, in situ measurements of local flow fields are challenged by animal avoidance of instrumentation inserted in the water column in their vicinity (Benoit-Bird & Lawson, 2016).

Magnetometry has emerged as a promising alternative to traditional velocimetry techniques (Tyler, 2006; Tyler et al., 1997) to quantify large-scale marine flows, including vessel wakes (Zou & Nehorai, 1998), tsunami detection and parameterization (Lin et al., 2021; Minami et al., 2021; Zhang et al., 2014), wave measurements (Davis, 1991; Podney, 1975), and ocean current profiling (Filloux, 1973; Lilley & Weitemeyer, 2004; Longuet-Higgins et al., 1954). Instead of measuring the velocity field directly, these magnetic techniques measure the flow-induced magnetic fields that naturally arise when electrically conductive fluids, such as seawater, move through a magnetic field, such as the Earth's geomagnetic field (Faraday, 1832; Podney, 1975; Tyler

et al., 1997, 2003). In contrast to traditional velocimetry approaches, which measure localized quantities such as fluid parcel displacement, the flow-induced magnetic field is an inherently nonlocal feature related to integrated properties of the fluid flow. Importantly, flow-induced magnetic fields can potentially be detected remotely at a distance from the region of moving fluid.

Recent simulations have suggested that turbulence generated by vertically migrating aggregations should also have a small, yet detectable magnetic signature (Dean & Soloviev, 2019). While the flow-induced magnetic signatures are typically several orders of magnitude smaller than the Earth's geomagnetic field strength, measurement of such signals is increasingly feasible due to rapid advances in the sensitivity, resolution, and availability of modern magnetometry techniques, especially quantum magnetometry techniques (Dang et al., 2010; Wolf et al., 2015).

In this Letter, a new approach is proposed to overcome the limitations of conventional velocimetry techniques in quantifying vertical transport due to migrating aggregations via their distinct magnetic signatures. By scaling the electromagnetic field equations, the leading order dynamics that govern the magnetic perturbation created by a vertically migrating aggregation are derived and found to depend on the induced velocity field through a Poisson equation. Using this relationship, two representative models for the biologically induced velocity field are analyzed to predict the behavior of the corresponding flow-induced magnetic field. The first model is representative of high aspect ratio aggregations, such as those encountered in laboratory experiments (Fu et al., 2021; Houghton & Dabiri, 2019; Houghton et al., 2018; Wilhelmus & Dabiri, 2014). In contrast, the second emulates the wider, low aspect ratio configurations observed in the field (Sato et al., 2013; Wiebe et al., 1979).

Across both models, common features of the magnetic signature are observed. In the presence of a horizontal geomagnetic field such as that found near the equator, each of these velocity field models generates a magnetic signature, **b**, that is poloidal, and whose vertical component has a strength proportional to the magnetic Reynolds number of the flow induced by the migration. Furthermore, the strength of this component is found to persist away from the aggregation and decay at a rate far slower than that of the corresponding velocity signature. Importantly, the magnetic signatures are predicted to be $\mathcal{O}(10-100$ pT), even at distances far removed from the aggregation (perhaps up to 1 km), which are potentially detectable with modern and emerging magnetometry techniques. Hence, magnetic detection of the migrations can potentially be accomplished without *a priori* knowledge of the precise location of the aggregation and without triggering animal avoidance from the introduction of measurement instruments into the migration (Benoit-Bird & Lawson, 2016).

2. Theory

2.1. Magnetic Field Equations

The motion of an electrically conducting fluid, such as seawater, through a magnetic field creates a corresponding electromagnetic signature. The electric current density, **j**, induced by the motion of seawater can be determined from the version of Ohm's Law given by

$$\mathbf{j} = \sigma\left(\mathbf{E} + \mathbf{u} \times \mathbf{B}_{\mathbf{geo}}\right), \tag{1}$$

where σ is the electrical conductivity of the seawater (3–6 S/m), **E** is any applied or induced electric field, **u** is the fluid velocity field, and $\mathbf{B}_{\mathbf{geo}}$ is the Earth's geomagnetic magnetic field (25,000–50,000 nT). The resulting electric current, **j**, creates a magnetic field perturbation, **b**, which can be determined from the magnetostatic version of Ampere's Law as

$$\nabla \times \mathbf{b} = \mu_0 \mathbf{j}. \tag{2}$$

Here, μ_0 denotes the magnetic permeability of seawater is taken to be equal to the magnetic permeability of free space ($\mu_0 = 4\pi \times 10^{-7}$ H/m).

When temporal variations in the geomagnetic field are assumed to be small compared to temporal variations in the magnetic perturbation (i.e., $\partial \mathbf{B}_{\mathbf{geo}}/\partial t \ll \partial \mathbf{b}/\partial t$), **E** in Equation 1 can be related to the motionally induced magnetic field perturbation, **b**, through the Maxwell-Faraday Law of Induction:

$$\frac{\partial \mathbf{b}}{\partial t} = -\nabla \times \mathbf{E}. \tag{3}$$

From the incompressibility of the fluid flow and Gauss's Law of Magnetism, the velocity field and magnetic fields, respectively, are solenoidal (i.e.,$\nabla \cdot \mathbf{b} = 0$, $\nabla \cdot \mathbf{B}_{\mathbf{geo}} = 0$, and $\nabla \cdot \mathbf{u} = 0$). Assuming σ to be constant over the domain of interest and combining the solenoidal constraints with Equations 1–3 gives the relation

$$\frac{\partial \mathbf{b}}{\partial t} = \frac{1}{\mu_0 \sigma} \nabla^2 \mathbf{b} + \left(\mathbf{B}_{\mathbf{geo}} \cdot \nabla\right)\mathbf{u} - (\mathbf{u} \cdot \nabla)\mathbf{B}_{\mathbf{geo}}. \tag{4}$$

Further simplification can be obtained by considering information related to the flows of interest. The leading order dynamics that determine $\mathbf{b}$ can be identified by replacing the variables in Equation 4 with dimensionless variables scaled by a characteristic dimensional prefactor. The magnitude of each prefactor is representative of the relevant oceanic context and flow of interest, that is, electrical conductivity ($\sigma = 5$ S/m), magnetic permeability ($\mu_0 = 4\pi \times 10^{-7}$ H/m), length scale ($L = 100$ m), and time scale ($T = 1$ hr). The dimensionless variables are denoted with an $\sim$ overline and given by $\tilde{t} = t/T$, $\tilde{\mathbf{b}} = \mathbf{b}/\beta$, $\tilde{\mathbf{r}} = \mathbf{r}/L = [x, y, z]/L = [\tilde{x}, \tilde{y}, \tilde{z}]$, and $\tilde{\mathbf{u}} = \mathbf{u}/U$, where β is magnetic field scale to be determined from the equations and $\mathbf{r}$ is the position vector. Substituting these variables into Equation 4 gives

$$\left[\frac{L\beta}{UT\left|\mathbf{B}_{\mathbf{geo}}\right|}\right]\frac{\partial \tilde{\mathbf{b}}}{\partial \tilde{t}} = \left[\frac{\beta}{\mu_0 \sigma L U \left|\mathbf{B}_{\mathbf{geo}}\right|}\right]\tilde{\nabla}^2\tilde{\mathbf{b}} + \left(\hat{\mathbf{B}}_{\mathbf{geo}} \cdot \tilde{\nabla}\right)\tilde{\mathbf{u}} - \left[\frac{\delta B_{geo}}{\left|\mathbf{B}_{\mathbf{geo}}\right|}\right]\left(\tilde{\mathbf{u}} \cdot \tilde{\nabla}\right)\hat{\mathbf{B}}_{\mathbf{geo}}. \tag{5}$$

where $\hat{\mathbf{B}}_{\mathbf{geo}}$ is the unit vector aligned with the geomagnetic field and δB_{geo} is the scale of the variations in geomagnetic field strength over the domain size, L. All dimensionless variables are outside the brackets and are of order unity if appropriately scaled, while the bracketed prefactors denote the scale of each term in Equation 5 and quantify their relative importance to the dynamics. This scaling analysis reveals that the first and last terms in Equation 5 are negligible for the flow of interest (see Supporting Information S1), such that the leading order dynamics in Equation 4 are governed by

$$\nabla^2 \mathbf{b} = -\mu_0 \sigma \left(\mathbf{B}_{\mathbf{geo}} \cdot \nabla\right)\mathbf{u}. \tag{6}$$

Furthermore, based on the scale of the leading order terms, the magnetic field perturbation scale, β, is found to scale as $\beta \sim \mathrm{R_m}\left|\mathbf{B}_{\mathbf{geo}}\right|$, where $R_{\mathrm{m}} = \mu_0 \sigma U L$ is the magnetic Reynolds number of the induced flow. The resulting 3D Poisson Equation 6 can be solved using a free space Green's function through the integral relation

$$\mathbf{b}(\mathbf{r}) = \iiint_V \frac{-\mu_0 \sigma \left(\mathbf{B}_{\mathbf{geo}} \cdot \nabla\right)\mathbf{u}(\mathbf{r}')}{4\pi \left|\mathbf{r} - \mathbf{r}'\right|} \mathrm{d}^3 r'. \tag{7}$$

such that the magnetic signature, $\mathbf{b}$, can be determined from a given velocity field, $\mathbf{u}$, induced by an aggregation migrating through a geomagnetic field, $\mathbf{B}_{\mathbf{geo}}$.

2.2. Models for the Induced Flow Field

To determine magnetic signatures produced by vertical migrations, representative velocity fields are chosen for high and low aspect ratio configurations of migrating aggregations. The high aspect ratio model is analogous to observations in laboratory experiments involving induced vertical migrations of zooplankton aggregations (Fu et al., 2021; Houghton et al., 2018; Wilhelmus & Dabiri, 2014), where the velocity signature is confined to a narrow extent of the domain and configurations have a large vertical extent relative to their width. This velocity field is modeled as a homogeneous, unidirectional flow in the vertical (z) direction with Dirac delta distributions in the horizontal plane (i.e., xy-plane). For an aggregation centered on the domain origin, the induced velocity field is given by

$$\mathbf{u}(\mathbf{r}) = [u, v, w] = [0, 0, Q\delta(x)\delta(y)] \tag{8}$$

where Q is the vertical volume flux. Here, we alternatively express Q in terms of a centerline vertical velocity scale, W, and characteristic width, ς_0, in the limit of $\varsigma_0 \to 0$ and $W \to \infty$ such that $Q = 2\pi W \varsigma_0^2$ is finite.

The low aspect ratio model represents migrating aggregations that have a large width relative to their vertical extent as a thin, thrust-generating disk (i.e., an actuator disk) (Rankine, 1865) that is vertically climbing at a steady rate. This approach has been successfully applied to the induced velocity fields of rotors (Johnson, 1980),

wind turbines (Shapiro et al., 2018), and, more recently, individual hovering krill (Murphy et al., 2013) and swarms of vertically migrating *Artemia salina* (Houghton, 2019). The induced velocity field is modeled as a linearly expanding, vertical jet with a Gaussian velocity distribution in the horizontal directions. This expanding jet extends downstream from the aggregation position but minimally impacts the upstream fluid. Even though the wakes of the individual swimmers in the vertical migration are not resolved, the far-field effect of the aggregation (i.e., its effect on the surrounding fluid) should be well represented by the actuator disk model. In the frame of the migrating aggregation, the surrounding vertical velocity field for an aggregation centered on the domain origin climbing with an upward velocity, W_v, is given by

$$w(x, y, z) = -W_v - \Delta w(z) \frac{D^2}{8\varsigma_0^2} \exp\left(\frac{-\left(x^2 + y^2\right)}{2\varsigma_0^2 d_w(z)^2} \right), \tag{9}$$

where $\Delta w(z)$ is the vertical velocity surplus in the negative z (i.e., downward) direction along the jet centerline, D is the nominal width of the aggregation where $D \approx 4.225\varsigma_0$ (Shapiro et al., 2018), and $d_w(z)$ is the dimensionless spreading function of the jet as a function of distance downstream of the aggregation, which is modeled as a linear expansion similar to the Jensen wake model (Jensen, 1983) and is given by the function

$$d_w(z) = 1 + k_w \ln(1 + \exp(2(z - 1)/D)). \tag{10}$$

The jet expansion coefficient is set to $k_w \approx 0.08$ as from Shapiro et al. (2018), but can be adjusted without loss of generality. The corresponding centerline velocity surplus, Δw, that conserves vertical momentum in the aggregation jet is given by

$$\Delta w(z) = \frac{\Delta w_0}{d_w^2(z)} \frac{1}{2} \left[1 + \operatorname{erf}\left(z\sqrt{2}/D \right) \right] \tag{11}$$

where Δw_0 denotes the induced velocity at the center of the aggregation position. When available, estimates for Δw_0 can be obtained from in situ measurements (Cisewski et al., 2010, 2021; Omand et al., 2021) or estimated *a priori* from animal and aggregation parameters following the methodology of Houghton (2019) (see Equation 38 in Supporting Information S1). Determining the appropriate model parameters to describe a given migration will depend on the specific organisms within the migration as well as their swimming mode and remains an open area of research.

In each case, x and y are aligned with the geographic East-West and North-South directions, respectively, and z is aligned with the vertical. The geomagnetic field is also taken to be constant over the domain of interest without declination (B_x) and inclination (B_z) such that $\mathbf{B}(\mathbf{r}) = \left[0, B_y, 0\right]$. The same analysis can be applied to other locations using the methods developed presently.

3. Results

3.1. Structure of the Magnetic Signature

The high aspect ratio model given by Equation 8 can be solved analytically as

$$\mathbf{b} = \left[b_x, b_y, b_z\right] = \left[0, 0, \frac{y\, H\, B_y\, \mu_0\, \sigma\, Q}{2\pi\left(x^2 + y^2\right)\sqrt{H^2 + x^2 + y^2}} \right], \tag{12}$$

where $2H$ is the vertical height over which the velocity field is integrated. From the relative directions of the geomagnetic field and fluid velocity, the magnetic perturbation manifests as a vertical magnetic field, b_z. This component decays inversely with the distance from the velocity signature near the aggregation and the inverse square of the distance in the far field. Furthermore, the magnitude of b_z varies sinusoidally about the axis of the migration. While the above solution in Equation 12 is specific to the Dirac delta limit, it will be shown to capture behavior derived for the low aspect ratio model as well.

Contour maps of the vertical velocity for the low aspect ratio model are shown over the xy-plane and yz-plane in Figures 1a and 1b, respectively. The corresponding dimensionless vertical magnetic field, $\tilde{b}_z = b_z/(B_y \mathrm{R_m})$, is computed by numerically integrating Equation 7 and shown in Figures 1c and 1d, where B_y is the strength of

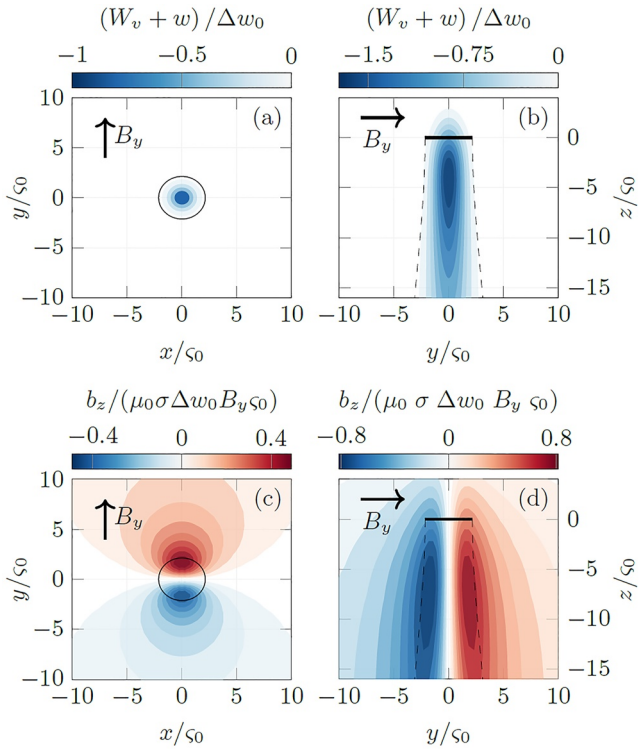

Figure 1. Contour plots of dimensionless velocity and magnetic fields. Solid black lines and circles represent the actuator disk of diameter, $D = 4.255\varsigma_0$, and dashed lines indicates the nominal width of the aggregation jet given by $Dd_w(z)$ in Equation 10. Panels (a and b) show contour plots of dimensionless vertical velocity ($(W_v + w)/\Delta w_0$) in the *xy*-plane and *yz*-plane, respectively. Panels (c and d) show corresponding contour plots of dimensionless vertical magnetic field component $\left(\tilde{b}_z = b_z/\left(\mu_0\sigma\Delta w_0 B_y \varsigma_0\right)\right)$ to panels (a and b). Here, $H = 50D$.

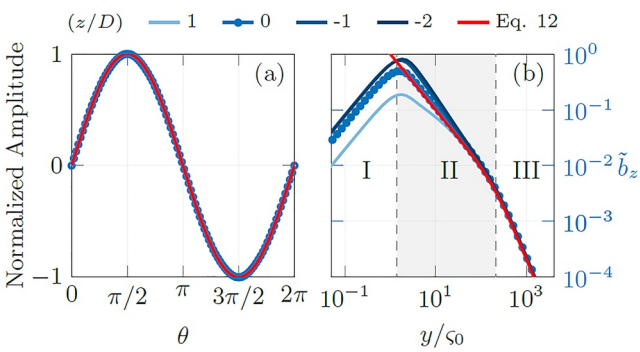

Figure 2. Profiles of dimensionless velocity and magnetic fields. (a) Normalized $\tilde{b}_z$ at a distance ς_0 from the aggregation center versus azimuthal position (θ) in the *xy*-plane ($z = 0$) relative to the positive *x*-axis for $x^2 + y^2 = \varsigma_0^2$. These correspond to normalized values obtained around the black circle in Figure 1c. (b) Variation of $\tilde{b}_z$ with distance along the *y*-axis (North-South direction). Blue lines/symbols are the vertical magnetic field signature computed from Equation 7 and red lines show Equation 12. Scaling regimes in panel (b) are highlighted by different shading. Here, $H = 50D$.

the North-South geomagnetic field component and, $R_m = \mu_0\sigma\Delta w_0\varsigma_0$ is the magnetic Reynolds number of the induced flow. Compared to the velocity signature given by equations Equations 9–11 (Figures 1a and 1b), the magnetic signature (Figures 1c and 1d) persists much further away from the location of the induced flow with a commensurate spreading of downstream of the aggregation location associated with the expansion of the velocity jet.

Similar to Equation 12, $\tilde{b}_z$ is also found to vary sinusoidally with azimuthal angle about the vertical axis, as shown in Figure 2a. However, the resulting magnetic signature from the more complex low aspect ratio model exhibits three distinct scaling regimes with horizontal distance, as shown in Figure 2b. Within the vicinity of the velocity signature (Region I in Figure 1d, $y/\varsigma_0 < 1$), the magnetic signature exhibits linear growth with distance from the migration axis due to collocation with the downwelling. In the region immediately outside the velocity signature (Region II, $y/\varsigma_0 > 1$) for $z = 0$, the magnetic perturbation decays inversely with distance from the migration (i.e., ς_0/y) until $y/\varsigma_0 \approx H/\varsigma_0$ where the signal begins to exhibit a stronger decay with the inverse square of the distance from the migration (Region III). By comparison, the decay of the magnetic signatures at downstream vertical locations downstream of the aggregation ($z < 0$ lines in Figure 2b) is slightly faster than the y^{-1} predicted by the high aspect ratio model.

3.2. Detectability of Biogenic Signatures

To assess the feasibility of detecting these magnetic signatures, representative values for each physical parameter are chosen and substituted for the dimensionless variables. Using $B_{geo} = 25\ \mu$T (Chulliat et al., 2020), $\varsigma_0 = 25$ m (Sato et al., 2013), $\sigma = 5$ S/m, and $\Delta w_0 = 1$ cm $\cdot s^{-1}$ (Cisewski et al., 2010, 2021; Omand et al., 2021), the nominal scale of the vertical magnetic signature gives $R_m B_y = \mu_0\sigma W\varsigma_0 B_y = 39$ pT. Recasting the data in terms of these parameters gives the distributions shown in Figures 3a and 3b for both the vertical velocity and magnetic components as a function of distance along the *y*-axis at various vertical locations. Superimposed on each distribution are the respective resolution/sensitivity limits for select measurement techniques for each parameter (see Tables S1 and S2 in Supporting Information S1 for a detailed tabulation of velocimetry and magnetometry techniques, respectively).

Common techniques for measuring velocity in the ocean such as Acoustic Doppler Current Profilers (ADCPs) (Nortek, 2021a, 2021c; Park & Hwang, 2021), Acoustic Doppler Velocimeters (ADVs) (Cisewski et al., 2010, 2021; Nortek, 2021b; Teledyne RD Instruments, 2009a, 2009b), and Particle Image Velocimetry (Bertuccioli et al., 1999; Jin, 2019; Katija & Dabiri, 2008; B. Wang et al., 2012) all have resolution limits close to a few millimeters per second. Consequently, these techniques are suitable for observing vertical currents from migrating aggregates of zooplankton, which are typically a few centimeters per second (Cisewski et al., 2010, 2021; Houghton et al., 2018; Omand et al., 2021; Wilhelmus & Dabiri, 2014). However, as seen in Figure 3a, the Gaussian decay of the induced flow with distance from the migrating aggregation (Equation 8) confines the usefulness of these techniques to the immediate vicinity of the velocity signature, with each reaching its sensitivity floor within a distance of $2\varsigma_0 - 4\varsigma_0$ of the aggregation center. Quantifying the bulk fluid transport due to the migration with these velocimetry techniques is conceptually straightforward and involves measuring the vertical velocity distribution within the jet core and spatially

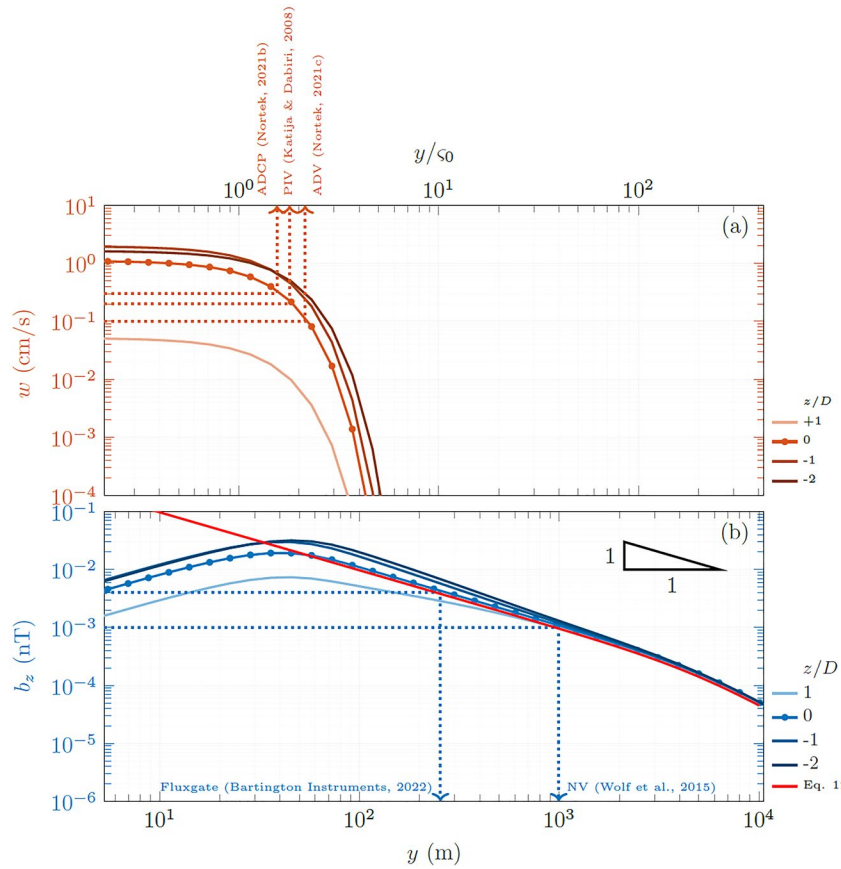

Figure 3. Profile of a representative dimensional (a) aggregation jet velocities and (b) corresponding vertical magnetic field strengths for the low aspect ratio model as a function of distance along the y-axis at different heights. Solid orange and blue lines show the vertical jet velocity and vertical magnetic field component, respectively, along the y-axis ($x = 0$) at vertical locations $z/D = -2, -1, 0$, and 1. Darker shades indicate lower heights, with the circles denoting the height of the aggregation itself. Dotted lines indicate the typical resolution or sensitivity limit of corresponding measurement techniques. The red line in panel (b) denotes Equation 12. Here, $H = 50D$.

integrating the results. However, in order to locate an instance of biogenic upwelling and downwelling via one of the localized velocimetry techniques (e.g., ADV), one would effectively need to be collocated with the aggregation, requiring *a priori* knowledge of its precise location and potentially triggering avoidance behaviors by the animals. This limitation is not as severe for ADCPs, which are capable of measuring linear velocity profiles over significant ranges, though it is still necessary for the interrogation volume to intersect with the flow induced by the aggregation in order to detect the biogenic flow.

In contrast, the magnetic field signature has the advantage of being detectable at distances far removed from the velocity jet, at distances potentially up to a kilometer away (see Figure 3b). This feature is enabled by the slow spatial decay of the magnetic signature coupled with the advancements in the capability of modern vector magnetometry techniques. For example, fluxgate magnetometers (Bartington Instruments, 2022; Magson GmbH, 2022; Metrolab Technology SA, 2022) and emerging quantum sensing techniques such as Nitrogen-vacancy centers (Wolf et al., 2015) have sensitivities on the order of $1 - 10\text{pT}/\sqrt{\text{Hz}}$, which are theoretically able to detect this magnetic signature almost an order of magnitude further away along the North-South axis than the velocimetry techniques considered above. Though absolute magnetometers are often much more sensitive than their vector counterparts, the vertical alignment of the magnetic perturbation relative to the horizontal field might preclude the use of such techniques in the scenario.

4. Conclusions

The persistence of the inverse decay of the induced magnetic field with distance from the aggregation facilitates a concise relationship through which the magnetic perturbation can be related to the biogenic upwelling

and downwelling. For magnetic field measurements obtained in the y^{-1} regime (Region II in Figure 2b), $\tilde{b}_z = b_z/(B_y\mu_0\sigma W\varsigma_0) = \varsigma_0 y/\left(x^2+y^2\right)$. Rearranging these terms reveals a new relationship for the volumetric flow rate driven by the migrating aggregation where

$$Q = 2\pi W\varsigma_0^2 = \frac{b_z}{B_y\mu_0\sigma}\frac{2\pi\left(x^2+y^2\right)}{y}. \tag{13}$$

In the above relationship, all properties of the aggregation and jet are contained on the left-hand side in the form of the volumetric flow rate. This quantity can be theoretically determined directly from suitable measurements of the magnetic perturbation, b_z, and its position relative to the aggregation (i.e., x and y) provided that the relevant environmental properties (i.e., B_y and σ) are known. Though a single measurement of b_z is theoretically sufficient, practical implementations may require mapping b_z over at multiple positions around the aggregation's location to adequately reject sources of magnetic noise unrelated to biogenic stirring. In the example presented above, a symmetric deployment of several magnetometers along the North-South direction allows for the rejection of common modes of magnetic noise with spatial scales larger than the induced magnetic signature, such as magnetic field variations induced by the tides. Such spatial arrangements can also be instrumental in identifying the predicted y^{-1} behavior. As demonstrated by Petereit et al. (2022), targeted temporal filtering can further enhance the signal-to-noise ratio of magnetic measurements in the ocean. The diel nature of the zooplankton migrations means that the resulting magnetic field will have temporal variations tied to a specific temporal scale (e.g., 24-hr) or an exogenous factor such as photosynthetically available radiation (Omand et al., 2021). Phase-locked measurements of the magnetic field measurements to this specific time scale or corresponding measurement of acoustic back-scattering, velocity, and photosynthetically available radiation can aid in distinguishing the resulting magnetic signal from other submesoscale phenomena and attributing it to the aggregation-derived stirring. While such filtering approaches may improve the signal-to-noise ratio, magnetic field measurements may still be susceptible to interference from the magnetic fluctuations induced in the ionosphere and potentially limit its applicability during periods of high solar activity (Constable, 2016; Petereit et al., 2022). Furthermore, Filloux (1973) found that while there are numerous and unique practical challenges related to instrument alignment and positional tracking for ocean-based measurement of magnetic fields, instruments with resolutions near 0.1 nT should be suitable for probing a diverse array of magnetic phenomena in the ocean including ionospheric activity. By complementing traditional tools with this new magnetic approach, it may finally be possible to quantify the significance of fluid transport and stirring in the ocean due to migrating aggregations of zooplankton. Moreover, this Letter presents a framework of testable predictions regarding the magnetic signatures of other oceanic phenomena that create analogous hydrodynamic signatures, such as geophysical sedimentation and propulsion of submarine vehicles.

Data Availability Statement

Further details and data regarding the theoretical derivations can be found in the Caltech Research Data Repository at https://doi.org/10.22002/0yha9-5qe05. MATLAB scripts and underlying computational results used in the figures for this manuscript are publicly available at https://github.com/mkfu/MagneticSignature.

Acknowledgments
This work was supported by the U.S. National Science Foundation (NSF) Alan T. Waterman Award.

References

Bartington Instruments. (2022). Mag-13 ® three-axis magnetic field sensors. Bartington Instruments Ltd 2023. Retrieved from https://www.bartington.com/products/high-performance-magnetometers/mag-13-three-axis/

Benoit-Bird, K. J., & Lawson, G. L. (2016). Ecological insights from pelagic habitats acquired using active acoustic techniques. *Annual Review of Marine Science*, *8*(1), 463–490. https://doi.org/10.1146/ANNUREV-MARINE-122414-034001

Bertuccioli, L., Roth, G. I., Katz, J., & Osborn, T. R. (1999). A submersible particle image velocimetry system for turbulence measurements in the bottom boundary layer. *Journal of Atmospheric and Oceanic Technology*, *16*(11), 1635–1646. https://doi.org/10.1175/1520-0426(1999)016<1635:aspivs>2.0.co;2

Chulliat, A., Brown, W., Alken, P., Beggan, C., Nair, M., Cox, G., et al. (2020). The US/UK World Magnetic Model for 2020–2025 (Tech. Rep.). https://doi.org/10.25923/ytk1-yx35

Cisewski, B., Hátún, H., Kristiansen, I., Hansen, B., Larsen, K. M. H., Eliasen, S. K., & Jacobsen, J. A. (2021). Vertical migration of pelagic and mesopelagic scatterers from ADCP backscatter data in the Southern Norwegian Sea. *Frontiers in Marine Science*, *7*, 1176. https://doi.org/10.3389/fmars.2020.542386

Cisewski, B., Strass, V. H., Rhein, M., & Krägefsky, S. (2010). Seasonal variation of diel vertical migration of zooplankton from ADCP backscatter time series data in the Lazarev Sea, Antarctica. *Deep Sea Research Part I: Oceanographic Research Papers*, *57*(1), 78–94. https://doi.org/10.1016/j.dsr.2009.10.005

Constable, C. (2016). Earth's electromagnetic environment. *Surveys in Geophysics*, *37*(1), 27–45. https://doi.org/10.1007/s10712-015-9351-1
Dabiri, J. O. (2009). Stirring by swimming bodies. *Geophysical Research Letters*, *37*(11), 11602–13490. https://doi.org/10.1016/j.physleta.2010.06.043
Dang, H. B., Maloof, A. C., & Romalis, M. V. (2010). Ultrahigh sensitivity magnetic field and magnetization measurements with an atomic magnetometer. *Applied Physics Letters*, *97*(15), 151110. https://doi.org/10.1063/1.3491215
Davis, C. A. (1991). *Magnetic fields generated by internal ocean seawater motion* (Unpublished doctoral dissertation). Naval Postgraduate School.
Dean, C., & Soloviev, A. (2019). Modeling the magnetic signature of diel vertical migrations of zooplankton. *OCEANS 2018 MTS/IEEE Charleston*, *2018*, 1–5. https://doi.org/10.1109/OCEANS.2018.8604488
Dewar, W. K., Bingham, R. J., Iverson, R. L., Nowacek, D. P., St. Laurent, L. C., & Wiebe, P. H. (2006). Does the marine biosphere mix the ocean? *Journal of Marine Research*, *64*(4), 541–561. https://doi.org/10.1357/002224006778715720
Faraday, M. (1832). VI. The Bakerian lecture. – Experimental researches in electricity. – Second series. *Philosophical Transactions of the Royal Society of London*, *122*, 163–194. https://doi.org/10.1098/rstl.1832.0007
Fernández Castro, B., Peña, M., Nogueira, E., Gilcoto, M., Broullón, E., Comesaña, A., et al. (2022). Intense upper ocean mixing due to large aggregations of spawning fish. *Nature Geoscience*, *15*(4), 287–292. https://doi.org/10.1038/s41561-022-00916-3
Filloux, J. H. (1973). Techniques and instrumentation for study of natural electromagnetic induction at sea. *Physics of the Earth and Planetary Interiors*, *7*(3), 323–338. https://doi.org/10.1016/0031-9201(73)90058-7
Fu, M. K., Houghton, I. A., & Dabiri, J. O. (2021). A single-camera, 3D scanning velocimetry system for quantifying active particle aggregations. *Experiments in Fluids*, *62*(8), 1–17. https://doi.org/10.1007/S00348-021-03256-X
Houghton, I. A. (2019). *Physical and biogeochemical impacts of migrating zooplankton aggregations* (Doctoral dissertation). Stanford University. Retrieved from http://purl.stanford.edu/qf211fm0762
Houghton, I. A., & Dabiri, J. O. (2019). Alleviation of hypoxia by biologically generated mixing in a stratified water column. *Limnology & Oceanography*, *64*(5), 2161–2171. https://doi.org/10.1002/lno.11176
Houghton, I. A., Koseff, J. R., Monismith, S. G., & Dabiri, J. O. (2018). Vertically migrating swimmers generate aggregation-scale eddies in a stratified column. *Nature*, *556*(7702), 497–500. https://doi.org/10.1038/s41586-018-0044-z
Huntley, M. E., & Zhou, M. (2004). Influence of animals on turbulence in the sea. *Marine Ecology Progress Series*, *273*, 65–79. https://doi.org/10.3354/MEPS273065
Jensen, N. O. (1983). *A note on wind generator interaction* (Tech. Rep.). Risø National Laboratory.
Jin, T. (2019). *Underwater particle image velocimetry (PIV) measurement of turbulence over mussel bed in a deepsite of Lake Michigan* (Unpublished doctoral dissertation). The University of Wisconsin-Milwaukee.
Johnson, W. (1980). *Helicopter theory*. Princeton University Press.
Katija, K., & Dabiri, J. O. (2008). In situ field measurements of aquatic animal-fluid interactions using a Self-Contained Underwater Velocimetry Apparatus (SCUVA). *Limnology and Oceanography: Methods*, *6*(4), 162–171. https://doi.org/10.4319/lom.2008.6.162
Kunze, E. (2019). Biologically generated mixing in the ocean. *Annual Review of Marine Science*, *11*(1), 215–226. https://doi.org/10.1146/annurev-marine-010318-095047
Kunze, E., Dower, J. F., Bevaridge, I., Bawey, R., & Bartlett, K. P. (2006). Observations of biologically generated turbulence in a coastal inlet. *Science*, *313*(5794), 1768–1770. https://doi.org/10.1126/SCIENCE.1129378
Lilley, T., & Weitemeyer, K. A. (2004). Apparent aeromagnetic wavelengths of the magnetic signals of ocean swell. *Exploration Geophysics*, *35*(2), 137–141. https://doi.org/10.1071/eg04137
Lin, Z., Toh, H., & Minami, T. (2021). Direct comparison of the tsunami-generated magnetic field with sea level change for the 2009 Samoa and 2010 Chile tsunamis. *Journal of Geophysical Research: Solid Earth*, *126*(11), e2021JB022760. https://doi.org/10.1029/2021JB022760
Longuet-Higgins, M. S., Stern, M. E., & Stommel, H. M. (1954). *The electrical field induced by ocean currents and waves, with applications to the method of towed electrodes*. Massachusetts Institute of Technology and Woods Hole Oceanographic Institution. https://doi.org/10.1575/1912/1064
Lorke, A., & Probst, W. N. (2010). In situ measurements of turbulence in fish shoals. *Limnology & Oceanography*, *55*(1), 354–364. https://doi.org/10.4319/lo.2010.55.1.0354
Magson GmbH. (2022). Digital fluxgate magnetometer. Retrieved from www.magson.de
Metrolab Technology SA. (2022). THM1176 and TFM1186 key specifications. Retrieved from https://www.metrolab.com/wp-content/uploads/2020/11/THM1176-TFM1186-Key-specifications.pdf
Minami, T., Schnepf, N. R., & Toh, H. (2021). Tsunami-generated magnetic fields have primary and secondary arrivals like seismic waves. *Scientific Reports*, *11*(1), 1–8. https://doi.org/10.1038/s41598-021-81820-5
Murphy, D. W., Webster, D. R., & Yen, J. (2013). The hydrodynamics of hovering in Antarctic krill. *Limnology and Oceanography: Fluids and Environments*, *3*(1), 240–255. https://doi.org/10.1215/21573689-2401713
Nortek. (2021a). Aquadopp 6000 m. Retrieved from https://www.nortekgroup.com/products/aquadopp-6000-m/pdf
Nortek. (2021b). Signature1000 current profiler. Retrieved from https://www.nortekgroup.com/products/signature-1000/pdf
Nortek. (2021c). Vector – 300m velocimeter. Retrieved from https://www.nortekgroup.com/products/vector-300-m/pdf
Noss, C., & Lorke, A. (2014). Direct observation of biomixing by vertically migrating zooplankton. *Limnology & Oceanography*, *59*(3), 724–732. https://doi.org/10.4319/lo.2014.59.3.0724
Omand, M. M., Steinberg, D. K., & Stamieszkin, K. (2021). Cloud shadows drive vertical migrations of deep-dwelling marine life. *Proceedings of the National Academy of Sciences*, *118*(32), e2022977118. https://doi.org/10.1073/pnas.2022977118
Park, H., & Hwang, J. H. (2021). A standard criterion for measuring turbulence quantities using the four-receiver acoustic Doppler velocimetry. *Frontiers in Marine Science*, *8*, 1128. https://doi.org/10.3389/fmars.2021.681265
Petereit, J., Saynisch-Wagner, J., Morschhauser, A., Pick, L., & Thomas, M. (2022). On the characterization of tidal ocean-dynamo signals in coastal magnetic observatories. *Earth Planets and Space*, *74*(1), 1–16. https://doi.org/10.1186/S40623-022-01610-9
Podney, W. (1975). Electromagnetic fields generated by ocean waves. *Journal of Geophysical Research*, *80*(21), 2977–2990. https://doi.org/10.1029/JC080I021P02977
Rankine, W. (1865). On the mechanical principles of the action of propellers. *Transaction of the Institute of Naval Architects*, *6*, 13–39.
Rousseau, S., Kunze, E., Dewey, R., Bartlett, K., & Dower, J. (2010). On turbulence production by swimming marine organisms in the open ocean and coastal waters. *Journal of Physical Oceanography*, *40*(9), 2107–2121. https://doi.org/10.1175/2010JPO4415.1
Sato, M., Dower, J. F., Kunze, E., & Dewey, R. (2013). Second-order seasonal variability in diel vertical migration timing of euphausiids in a coastal inlet. *Marine Ecology Progress Series*, *480*, 39–56. https://doi.org/10.3354/MEPS10215

Shapiro, C. R., Gayme, D. F., & Meneveau, C. (2018). Modelling yawed wind turbine wakes: A lifting line approach. *Journal of Fluid Mechanics*, *841*, R11–R112. https://doi.org/10.1017/jfm.2018.75

Simoncelli, S., Thackeray, S. J., & Wain, D. J. (2018). On biogenic turbulence production and mixing from vertically migrating zooplankton in lakes. *Aquatic Sciences*, *80*(4), 35. https://doi.org/10.1007/s00027-018-0586-z

Teledyne RD Instruments. (2009a). Ocean surveyor. Retrieved from www.teledynemarine.com

Teledyne RD Instruments. (2009b). Workhorse long ranger. Retrieved from www.teledynemarine.com

Tyler, R. H. (2006). Weak influences of the Earth's magnetic field on ocean circulation. *Geophysical Research Letters*, *33*(14), L14615. https://doi.org/10.1029/2006GL026372

Tyler, R. H., Maus, S., & Lühr, H. (2003). Satellite observations of magnetic fields due to ocean tidal flow. *Science*, *299*(5604), 239–241. https://doi.org/10.1126/SCIENCE.1078074/SUPPL_FILE/TYLER.SOM.PDF

Tyler, R. H., Sanford, T. B., & Oberhuber, J. M. (1997). Geophysical challenges in using large-scale ocean-generated EM fields to determine the ocean flow. *Journal of Geomagnetism and Geoelectricity*, *49*(11), 1351–1372. https://doi.org/10.5636/jgg.49.1351

Visser, A. W. (2007). Biomixing of the oceans? *Science*, *316*(5826), 838–839. https://doi.org/10.1126/SCIENCE.1141272/ASSET/7E1B4C1A-BCB2-4A76-8AC3-823DF065F9DD/ASSETS/GRAPHIC/838-1.GIF

Wang, B., Liao, Q., Bootsma, H. A., & Wang, P. F. (2012). A dual-beam dual-camera method for a battery-powered underwater miniature PIV (UWMPIV) system. *Experiments in Fluids*, *52*(6), 1401–1414. https://doi.org/10.1007/S00348-012-1265-9

Wang, S., & Ardekani, A. M. (2015). Biogenic mixing induced by intermediate Reynolds number swimming in stratified fluids. *Scientific Reports*, *5*(1), 17448. https://doi.org/10.1038/srep17448

Wiebe, P. H., Madin, L. P., Haury, L. R., Harbison, G. R., & Philbin, L. M. (1979). Diel vertical migration by *Salpa aspera* and its potential for large-scale particulate organic matter transport to the deep-sea. *Marine Biology*, *53*(3), 249–255. https://doi.org/10.1007/BF00952433

Wilhelmus, M. M., & Dabiri, J. O. (2014). Observations of large-scale fluid transport by laser-guided plankton aggregations. *Physics of Fluids*, *26*(10), 1–12. https://doi.org/10.1063/1.4895655

Wolf, T., Neumann, P., Nakamura, K., Sumiya, H., Ohshima, T., Isoya, J., & Wrachtrup, J. (2015). Subpicotesla diamond magnetometry. *Physical Review X*, *5*(4), 041001. https://doi.org/10.1103/PhysRevX.5.041001

Zhang, L., Baba, K., Liang, P., Shimizu, H., & Utada, H. (2014). The 2011 Tohoku tsunami observed by an array of ocean bottom electromagnetometers. *Geophysical Research Letters*, *41*(14), 4937–4944. https://doi.org/10.1002/2014GL060850

Zou, N., & Nehorai, A. (1998). Detection of ship wake using an airborne magnetic transducer. *Conference Record – Asilomar Conference on Signals, Systems and Computers*, *2*, 1316–1321. https://doi.org/10.1109/ACSSC.1998.751539